AIAA SciTech Forum
23-27 January 2023, National Harbor, MD & Online
AIAA SCITECH 2023 Forum

10.2514/6.2023-0260

Electrospray Emitter Geometry Characterization through Surface Profilometry and Parameter Estimation

Collin B. Whittaker* and Benjamin A. Jorns†
University of Michigan, Ann Arbor, MI, 48109

The geometries of the emitters and extractor apertures of an electrospray thruster array are experimentally characterized. Coherence scanning interferometry is employed to produce a topographic map of an 8×8 emitter region of a thruster array based on the 576-emitter AFET-2-type design. This interrogation region corresponds to a 4.4 mm $\times$ 4.4 mm $\times$ 0.5 mm volume and is captured at 0.35 μm resolution. The measurement domain is divided into 128 distinct sets of training data—one for each emitter and extractor imaged at the 64 sites. A geometric model based on key features such as emitter tip radius of curvature and extractor aperture diameter is fit to these subregions with a least squares algorithm. The resulting statistical distributions of these model parameters are reported over the 64 sites. It is found that parameters are near normally distributed, but are highly correlated and tend to have heavy tails corresponding to blunt emitters. Tolerances are found to vary between 0.16% for the aperture radius to 81% for the cone tip radius. The corresponding median tip radius of 23 μm is larger than the design specification, and this discrepancy is attributed to differences in the manufacturing methods employed. It is shown that this deviation from design can explain off nominal emission current of this array reported in previous work. The applications of the method for characterizing the emitter geometries are discussed, including their use as a means of characterizing tolerances in manufacturing processes and their value in learning and predicting emission nonuniformity via modeling under uncertainty.

Nomenclature

x, y	=	lateral coordinates
z	=	height coordinate
z_a	=	z position of the extractor aperture
r_{ex}	=	distance from aperture center
R_a	=	radius of extractor aperture
z_b	=	z coordinate of emitter chip basal plane
x_a, y_a	=	x, y coordinates of aperture center
z_c	=	z coordinate of emitter apex
R_c	=	radius of curvature of emitter tip
$r_e m$	=	distance from emitter center
α	=	emitter cone half angle
r_b	=	emitter base radius
x_c, y_c	=	x, y coordinates of emitter center
$(\cdot)_{ex}$	=	extractor subregion
$(\cdot)_{em}$	=	emitter subregion
i	=	site index
θ	=	model parameters
D	=	set of data
N	=	number of data in set
k	=	data index
F	=	model prediction

*PhD Candidate, Department of Aerospace Engineering, Student Member AIAA, cbwhitt@umich.edu
†Associate Professor, Department of Aerospace Engineering, Associate Fellow AIAA

h	=	emitter height
d	=	electrode gap distance
Δx	=	misalignment in x
Δy	=	misalignment in y
Δz	=	fit residual

I. Introduction

Nonuniform emission is a well documented phenomenon for electrospray thruster arrays. Experiments using small wire probes have revealed irregular ion beam structures [1–4], and post-operation inspections have shown asymmetric propellant deposition [5, 6]. This variation is undesirable not only as a reduction in performance (i.e. by wasting thruster mass and area on defunct emitters), but also because it increases the likelihood of a life-ending failure [7]. This problem is exacerbated by the need to aggregate many emitters in parallel for all but the smallest scale propulsive applications [8–12]. Understanding this nonuniformity is thus an imperative in continued electrospray development.

One potential source of inhomogeneity in emission is the geometry of the emitters and their extraction electrode. These influence every aspect of operation: the emitter body provides impedance that modulates fluidic transport [12–14], the emitter tip produces a local electric field which controls Taylor cone formation and ion evaporation [15–17], and the extractor geometry determines the optics for the resulting beam. Consequently, variability in this geometry (i.e. manufacturing tolerance) is integrally linked to the performance of an array [18].

Despite the importance of this irregularity in geometry, direct characterization of emitter arrays as manufactured is comparatively sparse in the literature, often limited to taking micrographs of a few emitters and fitting geometries by hand (i.e. superimposing a circle on the emitter tip to estimate its curvature). Such techniques may fail to adequately sample from the tolerances inherent to emitter fabrication, and they provide few avenues for rigorous uncertainty quantification. Given the potential losses in device performance and lifetime stemming from this variability, a more systematic characterization of emitter arrays post fabrication is warranted.

We present here a method for more comprehensive geometry measurements of an electrospray thruster array. This method is based on surface profilometry and model regression, and we apply it to a real electrospray thruster. We begin by describing the thruster article to be characterized and outlining the measurement method used to produce a topographic map of the thruster. We then formulate a model to parameterize the geometry of the system and develop a procedure for fitting this model to the data to estimate those parameters. We finally present the results of applying this procedure to a subsection of the thruster and describe these within the context of broader modeling and design efforts.

II. Methodology

We describe in this section the test article whose emitter and extractor geometries we examine, the key diagnostic technique used to resolve them, and the analysis methods to reduce those data into salient design parameters.

A. Thruster

We consider in this work the AFET-2 system, a design published by the Air Force to serve as a research testbed [9]. The AFET-2 thruster chip consists of 576 square pyramidal emitters, each ~300 μm tall. The emitters are conventionally machined on a mill from a porous borosilicate glass substrate and arranged in a rectangular grid ~1.6 cm^2 large. The emitters are formed by cutting a series of channels along the axes of the grid with a tapered endmill, leaving emitters in between. The version of the AFET-2 characterized in this work was manufactured at the University of Michigan and utilizes a novel resilient extractor architecture [6] rather than the standard AFET-2 extractor electrode. We note the machining parameters of [9], in particular the RPM of the cutting tool, could not be matched due to differences in machine setup. In testing in negative polarity using the ionic liquid 1-ethyl-3-metylimidazolium tetrafluoroborate (EMI-BF4), the thruster demonstrated emission up to -40 μA at -2450 V. We show a photograph of the thruster in Fig. 1.

B. Profilometery

To measure the thruster geometry, we use a coherence scanning interferometer, which operates by shining white light on the target through an interference objective. By examining the reflection's fringe pattern when recombined

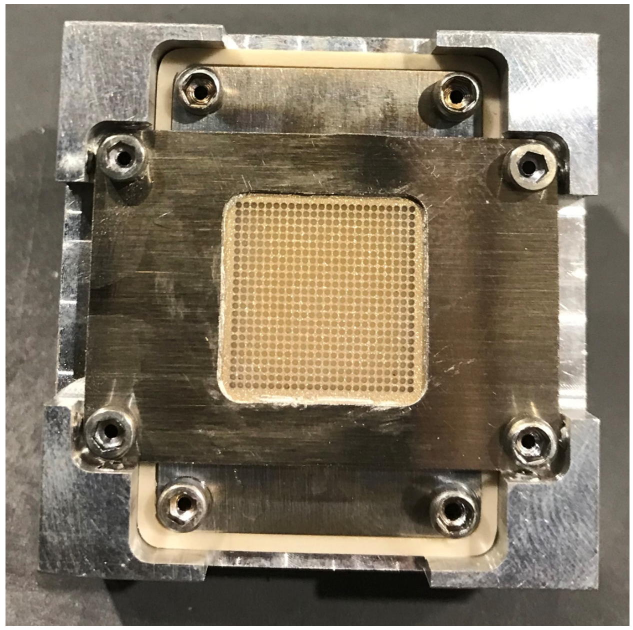

Fig. 1 Image of the AFET-2 test article at the University of Michigan.

with a reference beam, the distance between the sample and the objective can be determined with order 1 nm precision [19]. By further scanning the objective normal to the target and rastering laterally, a full 3D topographic map can be constructed. We provide a schematic diagram illustrating this process in Fig. 2. Using the interferometer, we map the surface topography in a 4.4 mm $\times$ 4.4 mm $\times$ 0.5 mm volume of the emitter chip. This is sufficient to resolve an 8×8 region of emitters from below their basal plane to above the top plane of the extractor. For the choice of objective, the field of view of the interferometer is 350 μm $\times$ 350 μm with a lateral resolution of 0.35 μm. This ultimately yields 2.5 megapixels per emitter.

C. Parameterizing emitter geometry

Our overarching goal in this study is to characterize the variability of the emitter geometry subject to manufacturing tolerance. To this end, we divide the domain into 64 individual sites, each containing one emitter and its corresponding extractor aperture. These sites are further subdivided into separate emitter and extractor domains. We introduce a common geometric model to parameterize each measured emitter and extractor geometry through a few key dimensions. We show notional diagrams of the side and top view of an arbitrary site subject to this parameterization in Fig. 3.

For the topography of the extractor aperture, we assume a circular pit within a plane:

$$z = \begin{cases} z_a, & r_{ex} \geq R_a, \\ z_b, & \text{otherwise}, \end{cases} \tag{1}$$

$$r_{ex}^2 = (x - x_a)^2 + (y - y_a)^2, \tag{2}$$

where (x, y, z) are the coordinates in the (arbitrary) measurement frame of the profilometer, z_a is the z coordinate of the top surface of the extractor, R_a is the radius of the extractor aperture, r_{ex} is the lateral distance from the center of the aperture (x_a, y_a), and z_b is the z coordinate of the emitter chip basal plane. The emitter topography we model as a

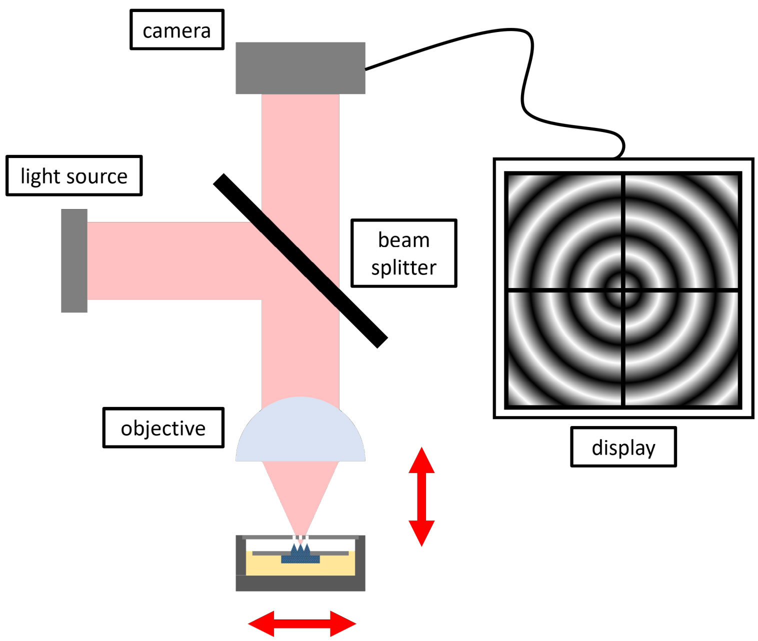

Fig. 2 Schematic illustration of coherence scanning interferometry, a surface profilometry technique

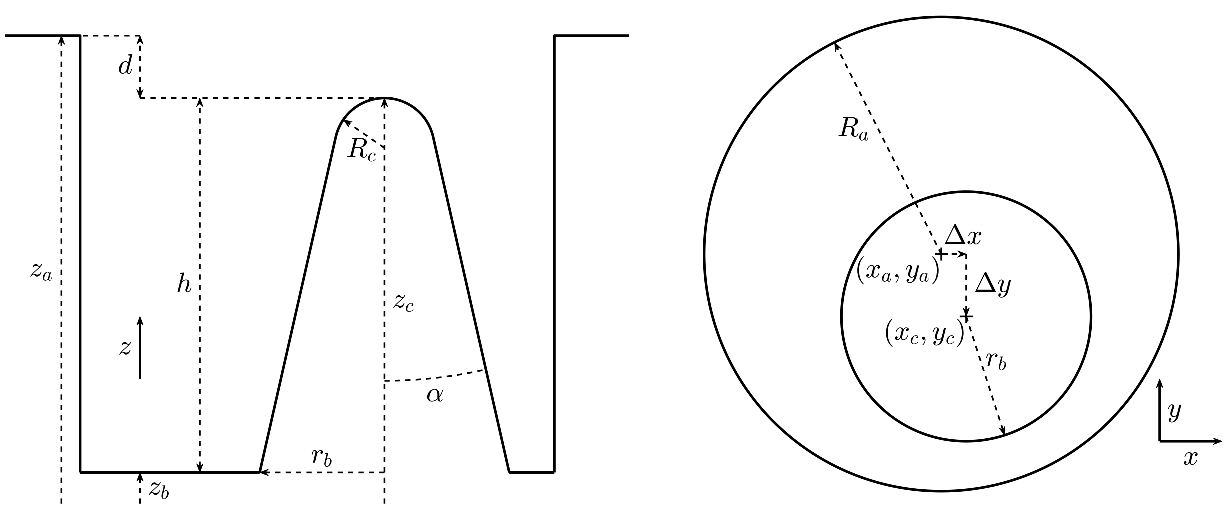

Fig. 3 Schematic diagram of side (left) and top (right) view of a site in the array, along with coordinate convention and key parameters of the geometric model

spherically-capped cone:

$$z = \begin{cases} z_c - R_c\left(1 - \frac{r_{em}^2}{R_c^2}\right), & r_{em} < R_c \cos\alpha, \\ (r_b - r_{em})\cot\alpha + z_b, & r_{em} \in [R_c \cos\alpha, r_b], \\ z_b, & \text{otherwise}, \end{cases} \tag{3}$$

$$r_{em}^2 = (x - x_c)^2 + (y - y_c)^2, \tag{4}$$

$$r_b = (z_c - z_b - R_c(1 - \sin\alpha))\tan\alpha + R_c \cos\alpha. \tag{5}$$

Here, z_c is the z coordinate of the cone apex, the top of the spherical cap, R_c is the radius of curvature of the cone tip, r_{em} is the lateral distance from the center of the cone (x_c, y_c), z_b is again the z coordinate of the emitter chip basal plane, α is the half-angle of the cone body, and r_b is the base radius of the cone. We note here that this representation is an expedience, since the emitters are pyramidal in practice.

D. Model regression

We seek finally to fit these models to the topographic data to determine the parameters of Eqs. (1) and (3). Consistent with our segmentation of the domain, we assume that the extractor $(\cdot)_{ex}$ and emitter $(\cdot)_{em}$ subregions of each of the $i = 1, 2, \ldots, 64$ sites is defined by its own independent set of parameters. The extractor geometries are defined by sets $\theta_{ex,i} = \left(z_{b,ex}, x_a, y_a, R_a, z_a\right)_i$, while the emitter geometries are defined by the sets $\theta_{em,i} = \left(z_{b,em}, x_c, y_c, z_c, R_c, \alpha\right)_i$. This treatment has the consequence that the basal plane $z = z_b$ will not be treated as constant between sites, or even between the emitter and extractor subregion of each site, hence the difference in notation. This is of little practical consequence, however, since the chip and interferometer may not be precisely parallel to begin with, and the absolute value of z_b is immaterial to our conclusions (see later discussion).

To determine the geometric parameters, we compute least-squares fits to the data. Associated with each subregion are data $D_{\{ex,em\},i}$, numbered $k = 1, 2, \ldots, N_{\{ex,em\},i}$. The least-squares fit to the parameters $\hat{\theta}_{\{ex,em\},i}$ is then given

$$\hat{\theta}_{\{ex,em\},i} = \underset{\theta_{\{ex,em\},i}}{\operatorname{argmin}} \sum_{k=1}^{N_{\{ex,em\},i}} \left(F_{\{ex,em\}}\left(x^{(k)}_{\{ex,em\},i}, y^{(k)}_{\{ex,em\},i}; \theta_{\{ex,em\},i}\right) - z^{(k)}_{\{ex,em\},i}\right)^2. \tag{6}$$

F here denotes the model-predicted value for z, which is a function of position (x, y) and the appropriate set of parameters θ. Given the nonlinearity and discontinuity of the geometry models, we use a Nelder-Mead method [20] to numerically determine the arguments of the minima.

III. Results

We present in this section key results form our measurement and analysis. We first show the measurements obtained with the profilometer, followed by example fits to a site in the grid, and finally statistics for the parameters over all sites.

A. Profilometry results

We show in Fig. 4 the full topographic map of the test volume. As can be seen, the emitters are primarily pyramidal and sit below the plane of the extractor electrode, being approximately centered in their respective apertures. Variations in geometry of the emitters are visible even at this scale, with some emitters being taller or shorter, some being more or less centered, and a small number having broken off wholesale from the emitter chip. Unexpected are the linear shelves stretching between emitters along the x axis. This is likely the result of using separate tools to cut the x and y channels, between which the cutting depth was not identical from error in the "touch-off" of the milling machine. Figure 5 shows an example at full measurement resolution of a single emitter, site 22 from Fig. 4. More evident at this scale is the detailed geometry of the cone tip, which is rounded (for this emitter) over a region order 50 μm wide. One can also distinguish surface roughness in the emitter basal plane, which is a combination of that inherent to the porous substrate and that introduced by the machining operation. The emitter subdomain for this site lies within the superimposed circle.

B. Single emitter and extractor model fits

These measurements in hand, we next apply our methodologies to estimate the geometries of all 64 sites of Fig. 4. When segmenting the domain into the corresponding 64 extractor regions and 64 emitter regions, we compute heuristic

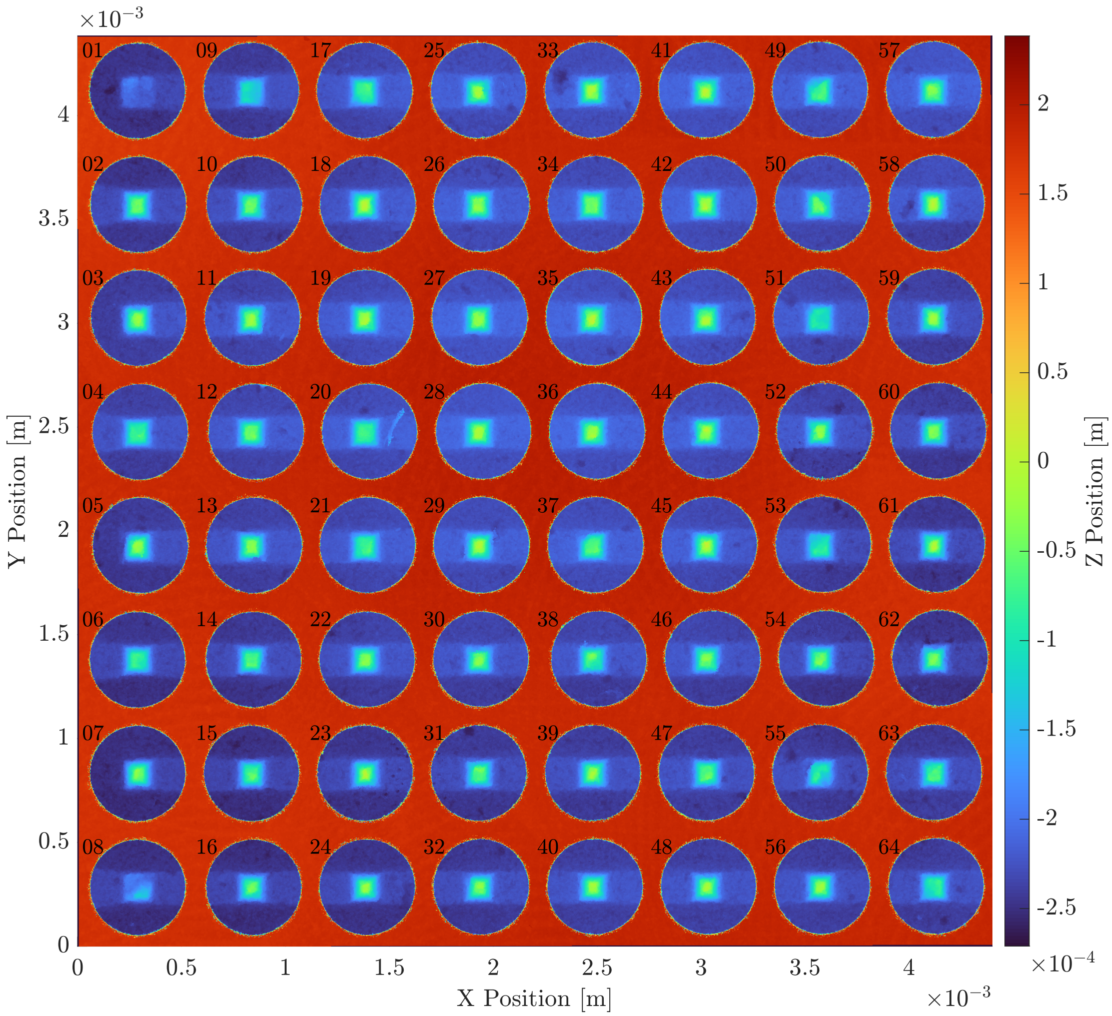

Fig. 4 3d topographic map of the 8×8 emitter grid of the AFET-2, with sites numbered

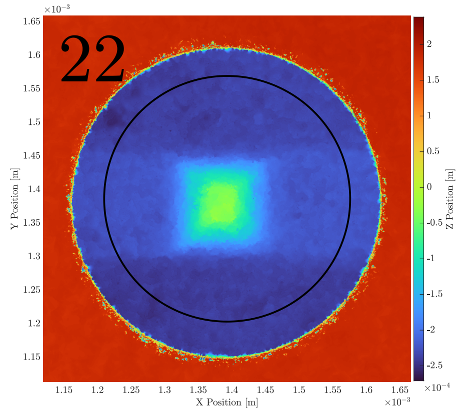

Fig. 5 Full-resolution 3d topographic map of a single site (22) from the AFET-2

initial estimates for the parameters (e.g. taking z_c as the highest z within the emitter domain). For each subregion, we initialize the minimizer with these estimates and then iterate until convergence (specified as a tolerance on the size of the simplex used in the method, cf. [20]).

We show in Fig. 6 an example fit to the emitter subregion for the site of Fig. 5. The top left shows a heatmap of the measurement of the profilometer, the top right is the same for the least-squares fit to the data, the bottom right shows the corresponding residual, and we collect the best fit parameters in the bottom left. As one can see, the model fits agree with the experimental data within ~5-10 microns for most of the domain, particularly near the apex of the emitter and in the basal plane surrounding them. The residuals are greater (order 25 microns instead) in the region corresponding to the shelf between emitters, and in a cross pattern apparent on the body of the emitter; the cross pattern forms because the emitters are square pyramids, rather than true cones as we have modeled here. The residual tends to be minimized when the predicted cone body lies between the corners and faces of the measurement, a consequence of its quadratic form: it is a lower penalty to match the corners and faces of the pyramid each with a medium error than it is to match one with a small error and the other with a large error.

We similarly show in Fig. 7 an example fit to the extractor subregion for the site from Fig. 5. The plot structure mirrors that of Fig. 6, with heatmaps of the measurement, the best fit, and the residual in the top left, top right, and bottom right, respectively, and the best-fit parameters again in the bottom left. The empty circle at the center of the domain corresponds to the emitter subregion. It is necessary to include a small amount of the emitter chip basal plane in order to resolve the aperture radius. For this result, the fit is also within ~5-10 microns for most of the domain, the exceptions being the same shelf in the basal plane noted previously for the emitter and the thin region surrounding the jump discontinuity at the edge of the aperture. The high residual at the edge of the aperture is expected since the aperture is not in practice perfectly circular (e.g. from chipping of the substrate during machining).

C. Emitter and extractor manufacturing statistics

Our goal in this section is to represent the 64 measured sites as a probability distribution over the geometric parameters and to compare these to the nominal design. To this end, we focus on the subset of parameters $(R_c, h, \alpha, d, R_a, \Delta x, \Delta y)$ (see Fig. 3), where in addition to the previously defined terms, we have introduced the quantities h as the height of the cone, d as the gap distance between the top surface of the extractor and the emitter apex, and Δx and Δy as the misalignment of the cone center from aperture center in the x and y directions, respectively. We compute these new parameters for each site from our existing model fits as

$$
\begin{aligned}
h_i &= z_{c,i} - z_{b,em,i}, && (7)\\
d_i &= z_{a,i} - z_{c,i}, && (8)\\
\Delta x_i &= x_{c,i} - x_{a,i}, && (9)\\
\Delta y_i &= y_{c,i} - y_{a,i}, && (10)
\end{aligned}
$$

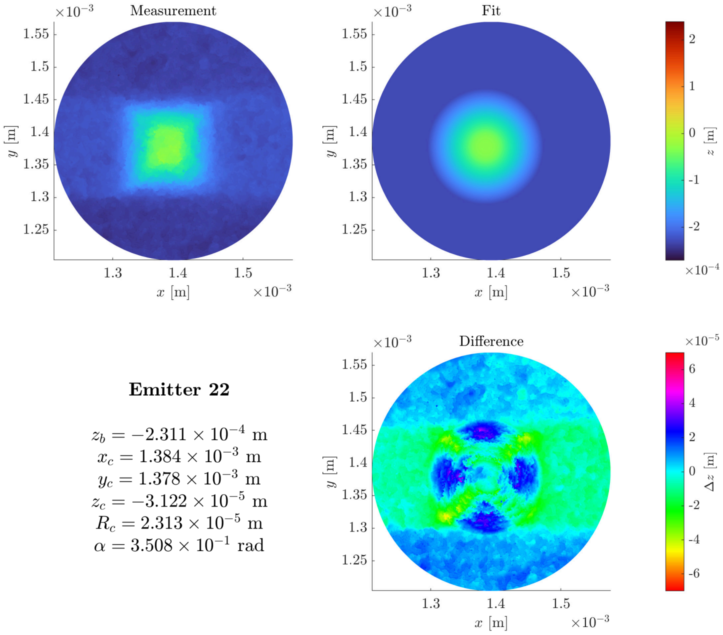

Fig. 6 Emitter subregion fit for an example site; top left: heatmap of the measurement, top right: heatmap of the least-squares fit, bottom left: best fit parameters, bottom right: heatmap of $\Delta z = F(x, y; \hat{\theta}) - z$; similar plots for all emitters are available here

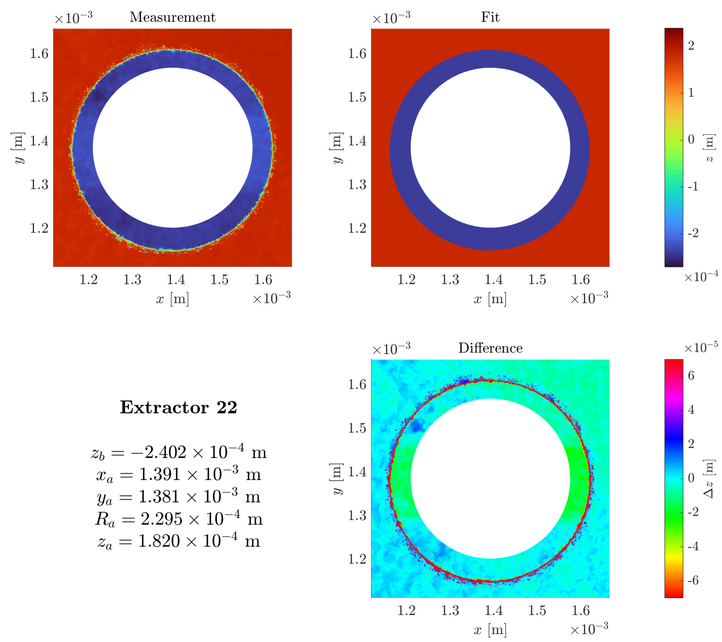

Fig. 7 Extractor subregion fit for an example site; top left: heatmap of the measurement, top right: heatmap of the least-squares fit, bottom left: best fit parameters, bottom right: heatmap of $\Delta z = F(x, y; \hat{\theta}) - z$; similar plots for all extractors are available here

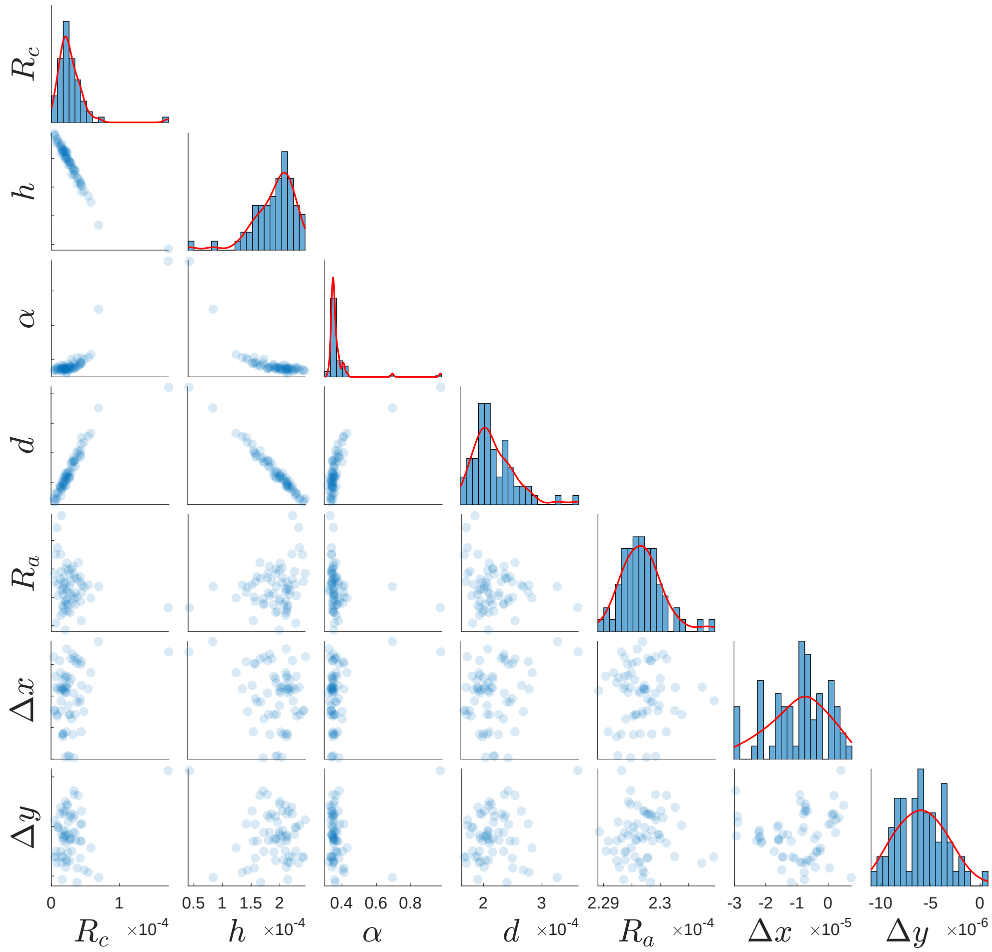

Fig. 8 Corner plot of site geometries; the diagonal entries are histograms for each parameter with a superimposed kernel density estimate to the population, while the off-diagonal entries are scatter plots over the 2d subspaces associated with each parameter; all units are in meters except α, which is in radians

where we note explicitly that we estimate the emitter height based on $z_{b,em}$ rather than $z_{b,ex}$ because it is only within the emitter subregion that the emitter geometry is modeled. We choose to focus on these parameters primarily because their nominal values have been examined previously for the AFET-2 and they have been invoked in simplified models for porous emitter performance[17, 18].

We collect the distribution of this new set of parameters over the 64 sites in Fig. 8 as a corner plot. This plot mimics the structure of a covariance matrix. For each parameter we plot a histogram of the values of that parameter over the 64 sites: these form the diagonal entries of the matrix. We also superimpose on these a kernel density estimate to the same population, assuming a Gaussian kernel. This serves to provide a smooth approximation to the distribution. Additionally, for each pair of parameters we plot their values over the 64 sites as scatter plots: these form the off-diagonal entries. Physically, this plot then represents the joint probability distribution of the parameters over all sites (i.e. the manufacturing tolerance in the emitters). We also tabulate key statistics of this population of sites in Tab. 1 alongside the nominal parameters for the AFET-2 system considered in [18]. These nominal parameters are based on the original design specifications for the AFET-2 reported in [9].

The narrow marginal distribution in R_a (standard deviation 0.16% of its mean) suggests that it is well-controlled during manufacturing, while the nonzero means of Δx and Δy suggest there is a bulk misalignment of the extractor to the emitter chip of order 10 microns. The discrepancy in R_a with respect to the nominal value exists because the resilient extractor was manufactured with smaller apertures to maintain structural integrity [6]. Whereas R_a and Δy

Parameter	Median	Standard Deviation	"Nominal" of [18]	Units
R_c	23.0×10^{-6}	22.7×10^{-6}	15.0×10^{-6}	m
h	199.5×10^{-6}	36.4×10^{-6}	301.8×10^{-6}	m
α	0.352	0.090	0.268	rad
d	209.0×10^{-6}	36.5×10^{-6}	3.0×10^{-6}	m
R_a	229.7×10^{-6}	0.4×10^{-6}	248.6×10^{-6}	m
Δx	-7.9×10^{-6}	9.2×10^{-6}	N/A	m
Δy	-6.0×10^{-6}	2.4×10^{-6}	N/A	m

Table 1 Median and standard deviation over the 64 sites along with the nominal parameters of [18]

appear to be normally distributed, the distribution in Δx appears clustered toward certain values, which suggests that something during the machining process changes the locality of several sites at once in x (e.g. backlash in the machine between cuts along successive rows). Furthermore, the aperture radius R_a and lateral misalignments Δx and Δy are largely independent from the other parameters and each other, evidenced by the fact that their joint distributions are scattered comparatively evenly across their domains. We expect this to be the case for R_a because the aperture is machined separately from the emitter, but the fact that this appears true for Δx and Δy indicates that the processes underlying variations in R_c, h, and α do not strongly change the location of the emitters in the grid.

More interesting are the strong correlations evident between R_c, h, d, and to a lesser extent α. These relationships are intuitive in that they reflect how much a cone has been blunted from the infinitely-sharp shape that would be left behind by an idealized cutting process (cf. [9]). The emitters have larger radii of curvature, R_c, and smaller height, h, the more blunt they are, explaining the negative correlation between these parameters. Similarly, they are spaced concomitantly farther away from the extractor, d, the shorter they are, since the offset of the extractor is fixed relative to the basal plane. This produces the negative correlation between h and d. These parameters tend to be near normally distributed, with the exception that they have tails correlating with larger radii of curvature. The extreme cases in the far tails (e.g. sites 1 and 8) where the emitters have broken off the basal plane wholesale suggest that a similar mechanism underlies this blunt tail in the distribution. The discrepancy between the nominal and measured α is explained partially by our parameterization of the geometry. The half-angle for the pyramid geometry is defined along its faces (i.e. by the taper of the cutting tool), and is therefore smaller than that of the best-fit conical body, as previously discussed. Similarly, the discrepancy in d is partially the result of the extractor electrode being fabricated to be thicker than intended [6]. However, even accounting for this, and noting the higher R_c and lower h values than nominal, these results decidedly indicate that the population of emitters examined here is blunter than for those reported previously.

Thus, we have produced a distribution over emitter geometries by first resolving a topographic map of the thruster and then fitting a geometric model to individual emitter and extractor regions. Doing so has not only allowed us to assess high-level manufacturing defects in the system like a ledge in the emitter chip basal plane, but also to understand the more subtle interrelationships that arise as consequences of the manufacturing methodology.

IV. Discussion

These results are illustrative of the utility of the present method for manufacturing characterization, that is, in identifying how changes in fabrication methods map to changes in emitter geometries. While qualitative assessments to this effect are simple to obtain (i.e. by looking at the thruster under a microscope), this analysis permits more precise comparison. For example, when we compare the geometries measured here to those shown notionally in [9], we conclude some combination of the change in machining parameters—tooling, "speeds and feeds", fixturing, etc.—has resulted in a median tip radius that is 8 microns larger and a median height 100 microns smaller. Of particular note here is the spindle speed, which [9] suggested played a key role in manufacturing success but was limited in production of this thruster—30000 RPM compared to the nominal 50000 RPM. By examining these and other relationships parametrically, we can begin to construct a quantitative model for the manufacturing process. This precision is a requirement as we seek to optimize manufacturing processes for tighter tolerance in emitter geometry, especially as the number of emitters in a system increases and requirements on emission uniformity may grow to ensure adequate device life [7].

This latter point highlights another major application of this analysis: in analyzing how deviations from nominal geometry stemming from these manufacturing processes map directly to changes in predicted performance. To this point, prior experiments with the thruster examined in this work attained substantially lower current yield compared to previous AFET-2 testing reported in the literature [6]. We hypothesized that the discrepancy could be explained if the electric field was weaker by a factor ~2.2, as might be caused by duller emitters. We have now quantified the geometries in this system and determined them to indeed be so. We now find that when we compute the electric field magnitude in the vicinity of the emitter tip for the median emitter of Tab. 1 by electrostatic simulation and compare it to the same for the nominal emitter geometry of [18], the discrepancy is a factor 2.1, suggesting this as the major source of the emission discrepancy.

By providing insight into the properties of the system as manufactured, this type of analysis is a critical tool for treating predictive models of these designs probabilistically. Indeed, we have previously shown through reduced-fidelity modeling that variability in geometry was necessary to reproduce the experimentally-measured current-voltage curve of an AFET-2 thruster [18]. Physically, this stemmed from the fact that different emitters were predicted to begin emitting at different voltages as a result of dissimilar electric field strengths at their apex, resulting in positive inflection in the emission current with voltage. In our previous analysis, however, we were forced to make major assumptions about the distribution of emitter geometries. We represented, for example, the manufacturing uncertainty as independent uniform or normal distributions, which is overly simplistic in light of the often highly correlated and heavy-tailed distributions of the current work. Even a partial resolution of a thruster, as presented here, serves to reduce this error and provides firmer grounding for the distribution in geometries otherwise assigned ad hoc. This probabilistic treatment of the emitter geometry forms a key component of conducting robust design over electrospray emitters, whereby we seek to identify new emitter designs that achieve specified performance targets with greater reliability [21].

Moreover, though our previous modeling work drew its conclusions through examination of the total current emitted by the thruster, these deductions are made potentially more powerful by intersection with methods that seek to infer individual emitter currents from spatially-resolved measurements (cf. [1, 22]). That is, if we are able both to estimate both the geometry of each emitter and the current it emits, we effectively modify a test on an array of emitters into many parallel tests of individual emitters, which could greatly accelerate model training.

The methods presented are not without limitation, however. For example, the measurement producing Fig. 4 took approximately 12 hours to complete on the profilometer, which may be impermissibly long in some contexts, especially for imaging an entire system (e.g. it would take 108 hours to image the full 24×24 grid of the AFET-2). This is driven largely by the small lateral spatial resolution (0.35 μm) and the long exposure times necessary to compensate for the translucence of the propellant-wetted emitter array. While it was sufficient for our purposes to allow the interferometer to complete the measurement overnight, we estimate taking a 1 μm resolution image of an unwet system could be around 20 times quicker.

The other potential refinement of this work is that we have not treated here any uncertainty in our estimates of the emitter geometries. We have implicitly taken them to be given deterministically by a least-squares fit to the parameters. This accounts neither for the magnitude of error in the data nor that inherent to the models Eqs. (1) and (3). Indeed, we find that for some emitters, the minimum found by the optimizer is sensitive to the initial estimate to the parameters, resolving to one of two modes with comparable values of the objective function. These estimates differ primarily in their tip radius R_c, and so we anticipate that this is a result of the dissimilar cutting depth in x and y during machining, producing correspondingly dissimilar radii of curvature along the two axes. To resolve this uncertainty we note that the least-squares fit implemented here is equivalent to a maximum likelihood estimate to the parameters within a Bayesian framework, assuming the data are Gaussian distributed with constant noise. Adopting the formalism of parameter estimation provides ready extensibility to more complete methods (e.g. sampling over the posterior distribution for the parameters using a Markov chain Monte Carlo method).

V. Conclusion

We have presented in this work a method for characterizing electrospray emitter geometry based in surface profilometry and parameter estimation. We were able to produce a topographic map of part of an electrospray thruster via coherence scanning interferometry, the map comprising 64 individual porous conical electrospray emitters and their associated extractor apertures over a 4.4 mm $\times$ 4.4 mm $\times$ 0.5 mm volume at 0.35μm resolution. We then parameterized the geometry of the emitters and extractors visible in this map and computed the parameters by least-squares fit. In so doing, we obtained a comparatively comprehensive characterization of the emitter geometries, including as distributions of parameters for relevant models predicting emission. We found that the population of emitters examined here disagreed with nominal values obtained for previous AFET-2 systems, in particular that the emitters were blunter, which may be explained by inferior tooling. We were also able to show that these blunter geometries resulted in an electric field at emitter apex a factor 2.1 times lower than the nominal, which agrees well with our hypothesis in previous work that the lower emission current yield of this thruster would be explained by electric fields weaker by a factor 2.2. Altogether, these methods and data represent a powerful tool in continued electrospray development, both in their ability to inform advances in manufacturing methods and in providing rigorous underpinning to future experiments and models that seek to understand and predict nonuniformity in electrospray emission.

VI. Acknowledgements

This work was supported by a NASA Space Technology Graduate Research Opportunity (80NSSC21K1247). The authors would like to thank Dr. Jon Mackey of NASA Glenn Research Center for his help in learning to operate the profilometer, the research staff of the Air Force Research Laboratory for their many insights, and Dr. Tom Liu of NASA GRC for his continued mentorship.

References

[1] Guerra-Garcia, C., Krejci, D., and Lozano, P., "Spatial uniformity of the current emitted by an array of passively fed electrospray porous emitters," *Journal of Applied Physics D*, Vol. 49, 2016, p. 115503.

[2] Courtney, D. G., Wood, Z., and Fedkiw, T., "Reconstructing Electrospray Plume Current Spatial Distributions using Computed Tomography," *36th International Electric Propulsion Conference*, 2019, p. 787.

[3] Fedkiw, T. P., Wood, Z. D., and Demmons, N., "Improved Computed Tomography Current Mapping of Electrospray Thrusters," *AIAA Propulsion and Energy 2021 Forum*, 2021, p. 3389.

[4] Wright, P. L., Uchizono, N. M., Collins, A. L., and Wirz, R. E., "Characterization of a Porous Tungsten Electrospray Emitter," *37th International Electric Propulsion Conference*, 2022, p. 232.

[5] Krejci, D., Mier-Hicks, F., Thomas, R., Haag, T., and Lozano, P., "Emission Characteristics of Passively Fed Electrospray Microthrusters with Propellant Reservoirs," *Journal of Spacecraft and Rockets*, Vol. 45, No. 2, 2017, pp. 447–458.

[6] Whittaker, C. B., and Jorns, B. A., "A Self-Healing Extractor for Electrospray Arrays," *International Electric Propulsion Conference 2022*, 2022 (in progress), p. 206.

[7] Jorns, B. A., Gorodetsky, A., Lasky, I., Kimber, A., and Dahl, P., "Uncertainty Quantification of Electrospray Thruster Array Lifetime," *International Electric Propulsion Conference*, 2019, p. 317.

[8] Lozano, P. C., Wardle, B. L., Moloney, P., and Rawal, S., "Nanoengineered thrusters for the next giant leap in space exploration," *MRS Bulletin*, Vol. 40, No. 10, 2015, p. 842–849.

[9] Natisin, M. R., Zamora, H. L., McGehee, W. A., Arnold, N. I., Holley, Z. A., Holmes, M. R., and Eckhardt, D., "Fabrication and characterization of a full conventionally machined high-performance porous-media electrospray thruster," *Journal of Micromechanics and Microengineering*, Vol. 30, 2020, p. 115021.

[10] Legge, R. S., and Lozano, P. C., "Electrospray Propulsion Based on Emitters Microfabricated in Porous Metals," *Journal of Propulsion and Power*, Vol. 27, No. 2, 2011, pp. 485–495.

[11] Krejci, D., Mier-Hicks, F., Fucetola, C., Lozano, P., Schouten, A. H., and Martel, F., "Design and Characterization of a Scalable Ion Electrospray Propulsion System," *International Electric Propulsion Conference*, 2015, p. 149.

[12] Cisquella-Serra, A., Galobardes-Esteban, M., and no, M. G.-C., "Scalable Microfabrication of Multi-Emitter Arrays in Silicon for a Compact Microfluidic Electrospray Propulsion System," *ACS Applied Material Interfaces*, Vol. 14, 2022, pp. 43527–43537.

[13] Courtney, D. G., and Shea, H., "Influences of porous reservoir Laplace pressure on emissions from passively fed ionic liquid electrospray sources," *Applied Physics Letters*, Vol. 107, 2015, p. 103504.

[14] Coffman, C. S., Martínez-Sánchez, M., and Lozano, P. C., "Electrohydrodynamics of an ionic liquid meniscus during evaporation of ions in a regime of high electric field," *Physical Review E*, Vol. 99, 2019, p. 063108.

[15] Coffman, C., Martinez-Sanchez, M., Higuera, F., and Lozano, P. C., "Structure of the menisci of leaky dielectric liquids during electrically-assisted evaporation of ions," *Applied Physics Letters*, Vol. 109, No. 23, 2016, p. 231602.

[16] Gallud, X., and Lozano, P. C., "The emission properties, structure and stability of ionic liquid menisci undergoing electrically assisted ion evaporation," *Journal of Fluid Mechanics*, Vol. 933, 2022, p. A43.

[17] Whittaker, C. B., and Jorns, B. A., "A Multi-site Emission Model for Porous Electrospray Emitters," *International Electric Propulsion Conference 2022*, 2022 (in progress), p. 205.

[18] Whittaker, C. B., Gorodetsky, A. A., and Jorns, B. A., "Model Inference on an Electrospray Thruster Array," *AIAA 2022 SciTech Forum*, 2022, p. 0041.

[19] de Groot, P., "Principles of interference microscopy for the measurement of surface topography," *Advances in Optics and Photonics*, Vol. 7, 2015, pp. 1–65.

[20] Nelder, J. A., and Mead, R., "A Simplex Method for Function Minimization," *The Computer Journal*, Vol. 7, 1965, pp. 308–313.

[21] Gorodetsky, A., Whittaker, C. B., Szulman, A., and Jorns, B., "Robust Design of Electrospray Emitters," *AIAA Propulsion and Energy 2021 Forum*, 2021, p. 3422.

[22] Jia-Richards, O., and Lozano, P. C., "Ensemble Kalman Update for Inference of Spatial Uniformity of Emission across an Electrospray Array," *43rd IEEE Aerospace Conference*, 2022, pp. 1–8.